**Local translation is required for sustained circuit integrity in impaired Wallerian degeneration**

Maria Paglione[1,+], Leonardo Restivo[1], Sarah Zakhia[2], Arnau Llobet Rosell[1], Marco Terenzio[2] and Lukas J. Neukomm[1,*]

[1] Department of Fundamental Neurosciences, University of Lausanne, 1005 Lausanne, Switzerland.

[2] Molecular Neuroscience Unit, Okinawa Institute of Science and Technology Graduate University, Kunigami-gun, Okinawa 904-0412, Japan.

[+] Lemanic Neuroscience Doctoral School (LNDS)

* Correspondence:
lukas.neukomm@unil.ch
+41 21 692 52 88

**Abstract**

After injury, the axon separated from the soma activates an evolutionarily conserved pathway to initiate its degeneration within a day. Attenuation of this pathway results in morphologically preserved severed axons and synapses for weeks after injury. When evoked, these projections remain able to elicit a postsynaptic behavior, a phenomenon that we define as preserved circuit integrity. The mechanism enabling the preservation of circuit integrity is currently unknown. Here we demonstrate that dNmnat-mediated over-expression potently blocks programmed axon degeneration in *Drosophila*. Thus, severed axons and their synapses of distinct sensory neuron populations remain morphologically preserved and circuit-integrated for at least a week. We used ribosomal pulldown to isolate translatomes from these severed projections. Transcriptional profiling revealed several enriched biological classes. Identified candidates were assessed by the quantification of evoked antennal grooming behavior as proxy for preserved circuit integrity. We identified mediators of local protein synthesis, and specifically candidates involved in protein ubiquitination and calcium homeostasis required for the preservation of circuit integrity by RNAi-mediated knock-down. Our dataset uncovered several uncharacterized genes linked to human disease and may therefore offer insights into avenues for therapeutic treatments.

## Introduction

Wallerian degeneration is a simple and well-established system to investigate how damaged axons execute their destruction (Waller, 1850). Upon axonal injury (axotomy), the axon separated from the soma employs programmed axon degeneration to initiate its degeneration within a day. The resulting axonal debris is cleared by phagocytosis through neighboring glial cells in subsequent days (Raiders et al., 2021; Sapar & Han, 2019). Programmed axon degeneration is evolutionarily conserved across species and appears to be hijacked in the absence of injury in several neurological conditions (Coleman & Höke, 2020; Llobet Rosell & Neukomm, 2019).

In *Drosophila*, four genes and a metabolite have been identified to mediate programmed axon degeneration(Fang et al., 2012; Llobet Rosell et al., 2022; Neukomm et al., 2017; Osterloh et al., 2012; Paglione et al., 2020; Xiong et al., 2012). *Drosophila* nicotinamide mononucleotide adenylyltransferase (dNmnat) is synthesized in the soma and transported into the axon. Axonal dNmnat levels are dictated by axonal transport and degradation mediated by the E3 ubiquitin ligase Highwire (Hiw). The remaining axonal dNmnat consumes the substrate nicotinamide mononucleotide (NMN) to generate nicotinamide adenine dinucleotide ($NAD^+$) in an ATP-dependent manner. Upon injury, the axonal transport of dNmnat is abolished. Consequently, dNmnat rapidly decreases, and with it, NMN consumption and $NAD^+$ synthesis. The resulting increase of NMN activates *Drosophila* Sterile Alpha and TIR Motif-containing protein (dSarm), a NADase that depletes axonal $NAD^+$. Low $NAD^+$ results in the degeneration of the injured axon mediated by Axundead (Axed).

A failure to activate programmed axon degeneration due to several genetic or metabolomic interferences results in severed projections that remain morphologically preserved for months. When evoked, they can elicit a postsynaptic behavior; an observation that we name preserved circuit integrity. For example, in mice deficient in programmed axon degeneration, for up to 5 days after injury, muscle fibers respond to severed, evoked motor axons (Mack et al., 2001). In *Drosophila* larvae, up to 24 h after injury, severed *hiw* motor axons continue to elicit evoked excitatory junction potentials (EJPs) and spontaneous mini EJPs (mEJPs) in muscles (Xiong et al., 2012). In adult *Drosophila* mutants for programmed axon degeneration, the evoked stimulation of severed grooming-inducing sensory neuron projections led to an antennal grooming behavior for at least two weeks after injury (Llobet Rosell et al., 2022; Neukomm et al., 2017; Paglione et al., 2020). Thus, programmed axon degeneration deficiency results in a potent preservation of circuit integrity. How this circuit integrity remains preserved (e.g., in the absence of cell body-derived support) is currently unknown.

The integrity of adult neurons and their long axons is essential for life-long nervous system function (Mariano et al., 2018). Axonal volume vastly exceeds the somatic one, and axons can

reach up to 20’000x the length of the neuronal cell body (Wedel, 2012). Thus, axonal local translation of mRNAs is one of the mechanisms contributing to axonal homeostasis in addition to cell body-derived transport of molecules and organelles (Holt et al., 2019; Ostroff et al., 2019; Yoon et al., 2012).

In Wallerian degeneration slow (*Wld*$^{S}$) mice, severed axons harbor an increased number of ribosomes after injury, suggesting a role for local protein synthesis (Court et al., 2008). However, applying protein synthesis inhibitors such as cycloheximide or emetine does not alter the preserved morphology in *Wld*$^{S}$; no discernible changes were evident even 72 h after injury (Gilley & Coleman, 2010). Therefore, the precise role of local protein synthesis in severed, preserved projections remains unclear. We hypothesized that local translation is required for preserved circuit integrity.

Here, we show that dNmnat-mediated over-expression potently blocks programmed axon degeneration for weeks after injury. Consequently, severed axons and their synapses of distinct sensory neuron populations remain morphologically preserved and circuit integrated. We used a ribosome pulldown to isolate translated transcripts one week after injury. In-depth transcriptional profiling revealed several enriched biological classes. We established a novel system to automatically quantify grooming behavior as proxy for preserved circuit integrity. Finally, several protein ubiquitination and calcium homeostasis candidates required for the preservation of circuit integrity were validated by RNAi-mediated knock-down.

## Results

### Preserved morphology and circuit integrity in severed axons with attenuated programmed axon degeneration.

We used a model deficient in Wallerian degeneration, which is well-explored in *Drosophila*, to isolate and explore the axonal and synaptic translatome (Llobet Rosell & Neukomm, 2019). After axonal injury, programmed axon degeneration is activated in the axon separated from its soma, resulting in axonal and synaptic degeneration within subsequent days. When programmed axon degeneration is blocked, severed axons and their synapses fail to degenerate and remain morphologically preserved for months (Osterloh et al., 2012; Neukomm et al., 2017). Notably, when evoked, these severed projections can release neurotransmitters to induce a postsynaptic behavior for weeks after injury (Xiong et al., 2012; Neukomm et al., 2017; Paglione et al., 2020). Here, we refer to this phenomenon as preservation of circuit integrity. Although local translation appears not to be required for the preservation of morphology (Gilley & Coleman, 2010), we sought to explore its requirement for circuit integrity.

The use of lethal mutants of programmed axon degeneration requires a clonal approach and significantly reduces the availability of biological material (Lee & Luo, 1999). We used tissue-specific over-expression of dNmnat (*dnmnat*$^{OE}$) to avoid this reduction. High levels of dNmnat should prevent a temporal rise of the prodegenerative initiation metabolite nicotinamide mononucleotide (NMN) by consuming NMN to catalyze nicotinamide adenine dinucleotide ($NAD^+$), thereby preventing the activation of programmed axon degeneration. (Llobet Rosell et al., 2022). First, we used *dnmnat*$^{OE}$ in ~20 *or22a*$^+$ GFP-labelled olfactory receptor neurons (ORN) (see genotype list for details). Their cell bodies are housed in 3$^{rd}$ antennal segments and project their axons into the antennal lobe of the central nervous system (CNS) (Vosshall et al., 2000). The bilateral ablation of 3$^{rd}$ antennal segments results in the removal of the cell bodies and the degeneration of ipsi- and contralateral axonal projections (MacDonald et al., 2006). We observed the degeneration of wild-type axons and subsequent progressive clearance of the resulting debris within 14 days post axotomy (dpa; e.g., post antennal ablation) (Figure 1A). In contrast, *dnmnat*$^{OE}$ axonal and synaptic morphology remained preserved at 7 and 14 dpa (Figure 1A). We quantified the percentage of antennal lobes with intact *or22a*$^+$ axons after injury (% axonal preservation) and found that axons remained fully preserved at 14 dpa. We also quantified the GFP-labeled projection area of axons and synapses and observed significant preservation at 14 dpa (Figure 1B). We confirmed our observations in ~40 *JO*$^+$ mechano-sensory neurons in the Johnston's Organ (JO). *JO*$^+$ cell bodies are housed in 2$^{nd}$ antennal segments and project their axons into the subesophageal zone of the CNS (Hampel et al., 2015, 2017). While the bilateral ablation of

2nd antennal segments resulted in the complete degeneration of wild-type *JO*$^+$ axons and their synapses, *dnmnat*$^{OE}$ axonal and synaptic morphology remained significantly preserved at 14 dpa (Figure 1C, D). Our observations suggest that *dnmnat*$^{OE}$ potently blocks the activation of programmed axon degeneration signaling, thereby preserving the morphology of severed axons and their synapses for weeks after injury.

Recently, we established a robust behavioral assay to assess preserved circuit integrity (Neukomm et al., 2017; Paglione et al., 2020). It relies on the *JO*$^+$ sensory input to activate the circuit of antennal grooming (Hampel et al., 2015, 2017). We expressed a red-shifted Channelrhodopsin (CsChrimson) in *JO*$^+$ neurons and dietarily supplemented *all*-trans retinal in food of all tested genotypes (Material and Methods). In wild type, optogenetics fails to induce antennal grooming after injury, as observed at 7 and 14 dpa. In contrast, *dnmnat*$^{OE}$ *JO*$^+$ neurons continued to elicit antennal grooming, to a similar extent at 7 dpa, and to a lesser extent at 14 dpa (Figure 1E). These results suggest that severed axons and their synapses with high levels of dNmnat remain circuit-integrated for at least one week after injury.

The abundance of protein synthesis is lower in dendrites and axons than in the soma (Glock et al., 2021). Therefore, we sought a Gal4 driver that labels an extended set of sensory neurons, whose cell bodies can be ablated like *or22a*$^+$ and *JO*$^+$ neurons. We identified the pan-ORN Gal4 driver olfactory receptor co-receptor (*orco–Gal4*) to manipulate ~800 ORNs (Vosshall et al., 2000; J. W. Wang et al., 2003). *orco*$^+$ cell bodies are housed in antennae and maxillary palps, and their axons project into the whole antennal lobe in the CNS. Bilateral antennal and maxillary palp ablation resulted in the degeneration and debris clearance of wild-type axons at 14 dpa. In contrast, severed *dnmnat*$^{OE}$ axons and their synapses remained significantly preserved (Figure 1F, G). These results further support that *dnmnat*$^{OE}$ is a potent tool to prevent axonal and synaptic degeneration for weeks after injury, regardless of the number of manipulated neurons. Since we focus on preserved circuit integrity, we decided to pursue with 7 dpa as time point to isolate the axonal and synaptic translatomes.

**Local axonal and synaptic translatomes of severed, preserved axons and their synapses one week after injury.**

The increase of manipulated tissue from ~20 *or22a*$^+$ to ~40 *JO*$^+$ to ~*800 orco*$^+$ neurons prompted us to test whether a GFP-tagged large ribosomal subunit protein RpL10Ab (GFP::RpL10Ab) can be detected and thus used for tissue-specific translating ribosome affinity purification (TRAP) (Thomas et al., 2012). While the Gal4/UAS-mediated expression of GFP::RpL10Ab did not result in a detectable GFP signal in *or22a*$^+$ nor *JO*$^+$ tissues, it could be detected in *orco*$^+$ tissues in Western blots derived from heads (Supplementary figure 1A, B). Thus, *orco*$^+$ tissues make it feasible to isolate axonal and synaptic translatomes in heads.

Next, we used the olfactory organs to perform tissue-specific TRAP (Figure 3A). Briefly, GFP::RpL10Ab was expressed in wild-type and *dnmnat*$^{OE}$ *orco*$^{+}$ olfactory organs. Both genotypes were subjected to antennal and maxillary palp ablations, and at 7 dpa, 300 heads collected each and snap-frozen in liquid nitrogen. Subsequently, axonal and synaptic-specific ribosomes/polysomes were immunoprecipitated with anti-GFP antibody-coated magnetic beads, mRNAs extracted, and reverse transcribed to establish cDNA libraries (Figure 2A, Material and Methods).

We identified 1033 differentially enriched axonal and synaptic transcripts in the two genotypes at 7 dpa, with 499 transcripts enriched in *dnmnat*$^{OE}$ (Figure 2B). These enriched transcripts, with a regularized logarithm (rLog) fold change value > 0.6 and a false discovery rate (FDR) < 0.05, were run through the database for annotation, visualization, and integrated discovery (DAVID) for gene ontology (GO) analyses of biological processes (Figure 2C). Notably, we observed a significant transcript enrichment of calcium transport ($p$ = 0.00017), axon extension ($p$ = 0.0004), axon guidance ($p$ = 0.002), RNA processing ($p$ = 0.007), as well as oxidation/reduction, ubiquitination, and transmembrane transport ($p$ = 0.03 each, respectively) (Figure 2C).

Since we compared the translatomes of *dnmnat*$^{OE}$ with wild type at 7 dpa, we wondered whether a genotype-specific GO term transcript enrichment is masking our results. Therefore, we included uninjured *dnmnat*$^{OE}$ and wild-type controls in our analyses. Interestingly, protein ubiquitination transcripts were enriched in *dnmnat*$^{OE}$ solely after injury (Figure 2D). In contrast, calcium transport transcripts were already enriched *before* injury, suggesting that it is likely a response to the expression of dNmnat (Figure 2D). We made a similar observation with transcripts related to axon guidance and extension, G-protein receptors, transmembrane transport, vesicle-mediated transport, autophagy, RNA processing, and 50 % of oxidative stress (Supplementary figure 2). Our initial analyses revealed the identification of enriched, genotype-independent and dependent transcripts of distinct biological GO terms.

A recent study examined *in vivo* mRNA decay in mammals by analyzing the axonal transcriptome in severed axons of *Sarm1*$^{-/-}$ knockout (KO) mice (Jung et al., 2023). mRNAs were collected from *Sarm1*$^{-/-}$ retinal ganglion cell (RGC) axons at 7 dpa and compared to naïve (uninjured) axons of the same genotype. Notably, while *Sarm1* mutant mice have a different genotype than *dnmnat*$^{OE}$ flies, both genotypes prevent the activation of programmed axon degeneration after injury (Fang et al., 2012; Gilley & Coleman, 2010; Osterloh et al., 2012). Thus, we compared the 7 dpa *Sarm1*$^{-/-}$ enriched axonal transcriptome with our 7 dpa TRAP *dnmnat*$^{OE}$ translatome. We discovered 61 enriched, orthologous mouse/fly transcripts in both datasets (Figure 2E). Importantly, our biological GO term analyses revealed an enrichment of transcripts related to protein polyubiquitination ($p$ = 0.009), calcium transmembrane transport ($p$ = 0.008), and transmembrane transport ($p$ = 0.042) (Figure 2F).

Our analysis of conserved orthologs revealed a common set of biological GO term transcripts enriched in mouse and fly after axonal injury.

We implemented another control to further restrict our analyses, where GFP::RpL10Ab was not expressed (*orco–Gal4* alone) (Supplementary figure 3A). We used this background control to filter wild type and *dnmnat*$^{OE}$ samples (both expressing GFP::RpL10Ab) (Supplementary figure 3B, C, D). The additional background filtering revealed a total of 165 transcripts *dnmnat*$^{OE}$ at 7 dpa, which were significantly lower than our initial dataset because of the more stringent filtering (Supplementary figure 3E). However, our biological GO term analyses revealed that most were similar to those found in the initial dataset (Supplementary figure 3F). Our combined analyses revealed that protein ubiquitination and calcium transport appear enriched in our local translatome datasets.

**A robust automated and high-accuracy antennal grooming detection system as a readout for preservation of circuit integrity.**

Next, we aimed to test whether the identified candidates were involved in preserving circuit integrity. However, the observation and manual scoring is time-consuming. Videos of flies with evoked antennal grooming behavior are analyzed manually on a frame-by-frame basis by an observer. Therefore, we decided to develop an automated system that performs a rapid and unbiased detection of antennal grooming behavior.

We designed a system consisting of two neural networks that allow frame-wise scoring of the movement of forelegs on the antennae, e.g., antennal grooming behavior. Briefly, the first network (Network 1) identifies the head region of the animal and enables the reduction of the analysis on a small area of the recording (Figure 3A). The second network (Network 2) uses this area and overlays three frames using pixel-wise standard deviations to generate a compressed image used for antennal grooming behavior detection (Material and Methods) (Figure 3A). The system was trained and validated to identify grooming or no-grooming events in these compressed images, resulting in a frame-wise probability of antennal grooming (Figure 3A). After training, the system produced probability scores similar to the manual scores of antennal grooming produced by the trained observer (Figure 3B).

To identify the probability cutoff where the quantification difference between the probability scores assigned by the system and the manual scores by the observer is minimal, the mean absolute differences were plotted in a probability-dependent manner using a novel test set. A minimal difference was observed with a probability ≥ 0.3 (Figure 3C). A linear regression between system and observer scores confirmed a strong correlation with a ≥ 0.3 probability cutoff (Figure 3D). Despite the > 93 % performance achieved by the system on the test set (Material and Methods), we compared the detection of antennal grooming from the system with the scores from the observer on newly recorded videos. Importantly, grooming detection

was not statistically significant between the system and the observer (Figure 3E). Our newly established two-network system provides plots of accurate probabilities of antennal grooming (Video 1).

Since our experiments are based on antennal injury, we observed that the presence or absence of antennae has a significant impact on the performance of network 2. We used a second, different training set comprised of videos where antennae were removed (e.g., at 7 dpa) to identify grooming or no-grooming events in the compressed images after injury. We repeated the same procedure with ablated antennae and determined a ≥ 0.4 probability cutoff where the difference between the system and the manual scores was minimal (Figure 3F). A linear regression between system and observer scores revealed a strong correlation (Figure 3G). We used newly recorded videos where antennal grooming detection was compared between wild type and *dnmnat*$^{OE}$ at 7 dpa with no statistical difference between the system and the observer (Figure 3H). Therefore, the system can also provide plots of accurate probabilities of antennal grooming after injury (Video 2, 3).

To further validate the accuracy of the automated system, we compared the grooming detection output of the system with manual scores obtained by two independent observers. We used a set of 24 novel raw videos of uninjured conditions. The output of the system was in line with both observers (Supplementary figure 4). It suggests the system produces scores in the natural variability range among observers.

We applied two distinct temperatures (20 and 25 °C) and red-light intensities (8 and 14 mW/cm$^2$), respectively, to test whether different experimental conditions affect grooming behavior. While red-light intensities had no impact, temperature-dependent nuances were identified by both the system and observer. Animals groomed significantly more at 25 °C (Supplementary figure 5).

We also used the system to track evoked grooming behavior from freshly born adults onwards, from 0 to 7 days post eclosion (dpe, with 14 mW/cm$^2$ at 25 °C). We observed a rise in evoked antennal grooming behavior with a plateau reached at 5 dpe (Supplementary figure 6). We conclude that the new system reliably detects nuances in evoked antennal grooming behavior and can be used to perform screens to identify changes thereof.

**RNAi-mediated knockdown of candidates involved in protein ubiquitination and $Ca^{2+}$ transport modify preserved circuit integrity.**

We used the newly established system to validate our transcriptomic dataset for synaptic integrity *in vivo*. We reasoned that RNA interference (RNAi)-mediated knockdown of candidates should not result in a phenotype before but specifically after axonal injury in severed *dnmnat*$^{OE}$ JO projections at 7 dpa. In this paradigm, while *dnmnat*$^{OE}$ animals harbor

a robust antennal grooming behavior, an RNAi-mediated reduction of candidate transcripts should result in an antennal grooming behavior phenotype (Figure 4A).

First, we focused on protein ubiquitination candidates. We tested 9 enriched candidates with RNAi, in uninjured *dnmnat*$^{OE}$ *JO*$^{+}$ neurons, and at 7 dpa. Interestingly, we observed three major phenotypes. First, several candidate RNAi experiments did not change grooming behavior, e.g., *pic*$^{RNAi}$ (Figure 4B, and supplementary figure 7). Second, a reduced grooming behavior was observed before and after after injury, e.g., *traf4*$^{RNAi}$ (Figure 4B). And third, grooming behavior was unaltered before, but reduced after injury, e.g., *huwe1*$^{RNAi}$ and the uncharacterized coding gene 10916 (*CG10916*$^{RNAi}$). RNAi-mediated knockdown of *CG6923* exhibited the strongest decrease in grooming behavior after injury (Figure 4B). Thus, our RNAi-mediated approach identified various protein ubiquitination genes that are required to sustain *dnmnat*$^{OE}$-mediated circuit integrity.

Disturbed calcium homeostasis in axons results often in their degeneration (Stirling & Stys, 2010). Thus, we assessed identified candidate transcripts involved in $Ca^{2+}$ transport across membranes. We observed the same major phenotypes as described above. Several candidate RNAi experiments did neither affect control nor injured antennal grooming behavior in *dnmnat*$^{OE}$, among them the knockdown of the pore-forming alpha$^{1}$ subunit D of the L-type voltage-gated $Ca^{2+}$ channel (*ca-alpha1D*$^{RNAi}$) and several others (Figure 4C, supplementary figure 8A). RNAi-mediated knockdown of *cacophony* (*cac*$^{RNAi}$) resulted in a reduced grooming behavior in control and injured *dnmnat*$^{OE}$ (Figure 4C). Knockdown of the endoplasmatic reticulum ryanodine receptor (*ryr*) important for the release of $Ca^{2+}$ from intracellular stores (*ryr*$^{RNAi}$) led to a decrease in grooming compared to *dnmnat*$^{OE}$ controls after injury, however, the decrease was not significant compared to its pre-injury control. In contrast, knockdown of the sodium/potassium/calcium exchanger *nckx30C* (*nckx30C*$^{RNAi}$) resulted in a reduced grooming behavior solely after injury (Figure 4C), observed with two different RNAi constructs (Supplementary figure 8B). Beyond the three phenotypes described above, we also identified the gene *CG32204* of unknown function, where *CG32204*$^{RNAi}$ resulted in an increase in grooming behavior after injury (Figure 4C). Our results provide evidence that calcium transport is crucial for sustained preservation of *dnmnat*$^{OE}$-mediated circuit integrity.

The RNAi-based validation of the identified transcripts by TRAP prompted us to ask whether a direct impairment of local translation also affects circuit integrity. We sought to test mTOR signaling, which is required for axonal local translation in nerve injury (Terenzio et al., 2018). Raptor is a component of the mTOR complex 1 (mTORC1) and regulates protein synthesis through ribosomal protein S6 kinase (S6k) (Figure 5A). Notably, *raptor* was enriched at 7 dpa in our dataset (Figure 2B). We targeted *raptor* and *s6k* by RNAi, and assessed their involvement in the preservation of *dnmnat*$^{OE}$-mediated circuit integrity. RNAi-mediated knockdown of *raptor* (*raptor*$^{RNAi}$) resulted in a decreased behavior before injury, and at 7 dpa,

we observed a statistically non-significant trend of a further decrease (Figure 5B). In contrast, *s6k*$^{RNAi}$ harbored an impaired circuit integrity phenotype as grooming behavior was reduced specifically after injury (Figure 5B). These results support our TRAP-mediated identification of transcripts locally translated in axons and their synapses. It appears that severed axons engage mTOR signaling-mediated local protein synthesis to ensure ubiquitin-mediated protein degradation to sustain amino acids for translation, and to combat calcium imbalance.

## Discussion

Here, we investigate how severed axons, deficient in programmed axon degeneration, employ local translation to sustain circuit integrity for at least one week after injury. We used the over-expression of *Drosophila* Nmnat (*dnmnat*$^{OE}$). dNmnat/NMNAT2 is an evolutionarily conserved enzyme essential for $NAD^+$ synthesis (Brazill et al., 2017; Zhai et al., 2009). It consumes NMN as a substrate to generate $NAD^+$ in an ATP-dependent manner, thereby preventing the initiation of programmed axon degeneration signaling.

Multiple studies have demonstrated the role of dNmnat/NMNAT2 in axons after injury (Fang et al., 2012). The discovery of the Wallerian degeneration slow (*Wld*$^S$) mouse provides the basis for our current understanding (Lunn et al., 1989). In *Wld*$^S$ mice, a complex genomic rearrangement led to the fusion of the N-terminal 70 amino acids of *Ube4b* and full-length *Nmnat1,* referred to as WLD$^S$, and thereby to the translocation from the nucleus to the axon. After axonal injury, in the severed axon, endogenous axonal NMNAT2 is rapidly degraded, while WLD$^S$ persists, resulting in preserved axonal morphology and circuit integrity (Mack et al., 2001).

In *Drosophila,* a previous study has demonstrated that the over-expression of dNmnat preserves axonal morphology for ~5 days after injury, by the use of an N-terminal Myc tagged dNmnat (Myc::dNmnat) (MacDonald et al., 2006). Here, we used an untagged dNmnat transgene (Zhai et al., 2006). Intriguingly, we observed a stronger morphological preservation, for at least two weeks, as tested in multiple neurons. The extended preservation may be attributed to untagged dNmnat, or to distinct insertion sites of the two separate transgenes, resulting in different expression levels.

Axons, which constitute most of the cytoplasm, are long and bridge the cell body to distant synapses. Despite the ~1 μm/s speed of axonal transport, in a 1 m human motor neuron, the cargo delivery from the cell body to the synapse requires approximately 12 days (Holt et al., 2019; Maday et al., 2014). Axonal transport alone cannot ensure rapid synaptic responses, but local axonal and synaptic translation of mRNAs can (Mariano et al., 2018; Ostroff et al., 2019; Yoon et al., 2012).

Remarkably, after injury, in the soma-attached axon, axonal regeneration is initiated through mTOR-mediated local axonal translation (Terenzio et al., 2018). More broadly, in regenerative tissue in axolotl (compared to non-regenerative tissue in mice), mTORC1 signaling mediates translation and tissue regeneration (Zhulyn et al., 2023). Therefore, ribosomes and local translation mediate regenerative responses. Surprisingly, severed *Wld*$^S$ axons which are separated from their soma harbor increased numbers of ribosomes (Court et al., 2008). They are organized into polysome clusters enclosed within multiple membrane

vesicles known as ribosome-containing vesicles (RVs), suggesting that local protein synthesis may be initiated (Court et al., 2008). We therefore hypothesized that the axon engages local protein synthesis to sustain itself. This appears in stark contrast with preserved *Wld*$^{S}$ axonal morphology that does not depend on local translation (Gilley & Coleman, 2010). Nevertheless, we revisited this question, but in the context of preserved circuit integrity.

Local mRNA translation in axons and synapses is less abundant than in cell bodies (Glock et al., 2021). To maximize the biological tissue for TRAP, we had to increase the number of manipulated axons and synapses. We sought a driver with two specific criteria: first, the Gal4 driver must label as many neurons as possible, and second, the ablation of cell bodies (e.g., injury) must not grossly affect the viability of animals. The pan-ORN driver *orco–Gal4* fulfills both criteria; it labels 800 olfactory receptor neurons with cell bodies housed in antennae and maxillary palps, which can be ablated without killing the animals. However, it is worth noting that after ablation, we observed an increase in mortality in wild-type animals at 14 dpa, but not in animals with *orco*$^{+}$ *dnmnat*$^{OE}$. Combined with the strong preservation of circuit integrity at 7 dpa, it prompted us to perform TRAP at 7 rather than 14 dpa.

Many locally transcribed mRNAs have already been described in pre- and postsynaptic compartments of neurons (Hafner et al., 2019). Among them the local translatome of retinal ganglion cells during development and in the adult mouse (Gumy et al., 2011; Jung et al., 2023; Shigeoka et al., 2016). Here, we identified around 500 enriched transcripts by TRAP. Interestingly, we isolated transcripts associated with RNA processing, specifically related to RNA binding activity. RNA binding proteins regulate mRNA axonal transport and local translation (Ederle & Dormann, 2017; Ishiguro et al., 2016; Thelen & Kye, 2020). For example, RNA-binding protein 4F (Rnp4F) encodes an evolutionarily conserved RNA-binding protein that plays a critical role in these processes. We also identified uncharacterized genes, *CG32533* and *CG1582*, which are predicted to possess RNA binding and helicase activity. Our findings thus add complexity to the understanding of RNA processing mechanisms, and local translation.

Our analysis revealed an array of transcripts associated with polyubiquitination. This enrichment was exclusively observed after injury. Ubiquitination is a marker for protein degradation crucial for the turnover of translated polypeptides (Ding et al., 2007; Jarome & Helmstetter, 2014; Patrick, 2006). In addition, a recent study in *Sarm1*$^{-/-}$ knockout axons assessed mRNA decay (Jung et al., 2023). In severed *Sarm1*$^{-/-}$ axons; mRNAs could be captured even one week after injury, revealing a comprehensive *Sarm1*$^{-/-}$ axonal transcriptomic profile (Jung et al., 2023). We took advantage of this dataset and identified potential shared mechanisms. Unexpectedly, transcripts linked to protein ubiquitination were

among the conserved fly/mouse candidates, further supporting that local protein synthesis is in place after injury.

The combination of identified conserved mouse/fly transcripts with a more stringent filtering approach revealed transcripts related to calcium transport and homeostasis. In line with our observations, elevated calcium levels can activate calpain proteases. Intriguingly, voltage-dependent sodium channels are among the targets of calpains. The channel degradation leads to an increase of axonal calcium, and culminates in axon degeneration(Iwata et al., 2004; Llobet Rosell & Neukomm, 2019; Rishal & Fainzilber, 2014).

Our identification of TRAP candidates and their subsequent assessment in the preservation of circuit integrity led us to speculate that protein synthesis forms the basis for sustained circuit integrity. We hypothesized that the mTORC1 pathway could act as a mediator in our assay. The mTORC1 pathway governs protein synthesis and tissue regeneration (Terenzio et al., 2018; Wang & Proud, 2006). Raptor and S6K are downstream mediators of the mTORC1 pathway for protein synthesis. Since we observed an increase in *raptor* transcripts in *dnmnat*$^{OE}$ at 7 dpa, it prompted us to conduct knockdown experiments targeting Raptor and S6K. The specific reduction of preserved circuit integrity after injury with *s6k*$^{RNAi}$ suggests an intricate involvement of the mTORC1 pathway in regulating circuit integrity through local translation.

After injury, the axon attached to the cell body employs local translation to initiate regeneration. Based on our overall observations, we propose that severed projection employ local protein synthesis through axonal/synaptic ribosomes, when programmed axon degeneration is inhibited. Among the translated transcripts are candidates that help to cope with the turnover of already translated polypeptides by polyubiquitination, and calcium buffering. This model is supported by the impairment of either local translation, or candidates related to calcium transport or polyubiquitination, resulting in a reduced circuit integrity.

Our comprehensive local translatome presents an intriguing avenue into distinct axonal and synaptic mechanisms, independent of cell body support. Our dataset identifies different uncharacterized genes linked to human disease that are associated with impaired axonal transport and local translation. *CG13531* is an enigmatic gene with implications in axon extension and synaptic vesicle transport. The human ortholog(s) have been linked Charcot-Marie-Tooth disease axonal type 2X, amyotrophic lateral sclerosis type 5, and hereditary spastic paraplegia 11, underlining its relevance in the neurodegenerative context.

Finally, it is worth noting that programmed axon degeneration is triggered by chemotherapeutic agents (Geisler et al., 2019; Krauss et al., 2020), and the deficiency of NMNAT2 is linked to a range of human diseases (Huppke et al., 2019; Lukacs et al., 2019). It

underscores the critical importance of these proteins in maintaining and protecting axonal projections. By focusing on the characterization of genes conserved among flies and mammals, it may lead to the identification of therapeutically targetable candidates slowing or even halting human axonopathies.

## Material and Methods

### Husbandry and genetics

*Drosophila melanogaster* was used to perform experiments. Animals were raised on Nutri-Fly Bloomington Formulation food at 25 °C on a 12h:12h light-dark cycle unless otherwise specified. Genotypes are listed in the genotype list.

### Axotomy-specific injury assays

Antennal-specific or antennal and maxillary palp ablation: Animals were aged for 5–10 days at 25 °C before axotomy (Paglione et al., 2020). Anesthetized animals were subjected to bilateral ablation of antennae or bilateral ablation of antennae and maxillary palps with high precision and ultra-fine tweezers. Animals were recovered in food-containing vials for a specified time.

### Brain dissection, immunohistochemistry, image acquisition and analysis

Adult brains were dissected at 7 and 14 days post axotomy (dpa) with the corresponding uninjured control, using a modification of a previously described protocol (Paglione et al., 2020). Decapitated adult heads were pre-fixed in 4 % paraformaldehyde (PFA) in 0.1 % Triton X-100 in 1x phosphate-buffered saline (PBS), pH 7.4 (PTX) for 20 min at room temperature (RT), and subsequently washed in PTX for 5 x 2 min. The dissection of the brains was performed in PTX, followed by brain fixation in 4 % formaldehyde in PTX for 10 min at RT. After fixation, the brains were washed in PTX for 5 x 2 min and blocked in 10 % normal goat serum (Jackson Immuno) in PTX (blocking solution) for 1 h at RT. Primary antibody incubation was performed in blocking solution containing 1:1000 chicken anti-GFP (Rockland) over night at 4 °C. Brains were washed with PTX for 3 x 10 min at RT and incubated with secondary antibodies in PTX (1:200 goat anti-chicken IgY H&L DyLight 488 (Abcam)) for 2 h at RT. Brains were washed with PTX for 3 x 10 min at RT and mounted in Vectashield. Images were acquired along the z-axis with a step size of 0.6 µm using a Nikon Spinning Disk confocal microscope. Image quantification was analyzed with ImageJ (NIH).

### Western blots

For each genotype, 20 adult heads were ground in 100 µl of Laemmli sample buffer (2 heads/10 µl) and heated for 10 min at 95 °C. 20 µl of the resulting lysate was loaded per well into 4-12 % SurePAGE™ gels (GeneScript) with MOPS running buffer for higher molecular weight proteins. Protein separation was carried out at 80 V. Precision Plus Protein™ Kaleidoscope™ Prestained Protein Ladder (Bio-Rad) was used as a molecular weight marker. The proteins were wet-transferred onto PVDF membranes (Bio-Rad) at 110 V for 70 min at

4 °C. Membranes were washed with Tris-buffered saline (TBS) containing 0.1 % Tween® 20 (Merk) (TBS-T) for 5 min at RT. Membranes were blocked with 5 % milk (Carl-Roth) in TBS-T for 1h at RT, and incubated in a blocking solution containing primary antibodies (1:5000 rabbit anti-GFP (Abcam), and 1:15000 mouse anti-Tubulin (Sigma)) over night at 4°C. Membranes were rinsed with TBS-T for 3 x 10 min and incubated with secondary antibodies in 5 % milk in TBS-T (1:10000 goat anti-rabbit IgG (H+L) Dylight 800, and 1:10000 goat anti-mouse IgG (H+L) Dylight 680 (ThermoFisher)) for 1 h at RT. Membranes were then rinsed with TBS-T for 3 x 10 min before signal acquisition. Fluorescent signals were acquired using Odissey® DLx (LI-COR), and image quantification was performed with ImageJ (NIH) through densitometric analysis.

**Translation Ribosome Affinity Purification (TRAP)**

Preparation of samples: The ribosomal pulldown was performed by adapting the already described protocol (Rozenbaum et al., 2018). In brief, for each genotype and condition, 300 adult animals were collected, snap-frozen in liquid nitrogen and stored at -80 °C before processing. The frozen samples were homogenized using 2-3 % weight per volume of homogenization buffer (100 mM KCl, 12 mM $MgCl_2$, 1 % NP-40, 50 mM Tris, pH 7.4) supplemented with β-mercaptoethanol (10 µl / ml buffer solution). The lysate was centrifuged at 10000 rpm for 10 min at 4 °C, and the supernatant was collected in a protein low-binding tube. 10 % was kept for the input and stored at -80 °C.

Preparation of beads: For each sample, 50 µl of magnetic agarose GFP-Trap beads were added to a RNase/DNase-free microcentrifuge tube. The beads were rinsed with homogenization buffer supplemented with 1 mM DTT, 150 µg/ml cycloheximide, 450 U/ml RNasin OUT, 10 mM ribonucleoside vanadyl complexes (RVC) and protease inhibitor (Sigma, P8340)).

GFP pulldown: The homogenized heads were incubated with magnetic agarose GFP-Trap beads to pulldown ribosomes with associated mRNAs at 4 °C over night. The beads were washed in high salt buffer (300 mM KCl, 12 mM $MgCl_2$, 1 % NP-40, 1 mM DTT, 150 µg/ml Cycloheximide, 450 U/mL RNasin OUT, protease inhibitor (Sigma, P8340), 50 mM Tris, pH 7.4) 3 x 5 min at 4 °C. Immediately after removing the final high salt wash buffer, samples were placed in a magnet, and 350 µl of lysis buffer was added to the beads (LB, RNA plus Kit for the inputs or LB1, RNA Plus XS kit, for the pulldowns). RNA was extracted from ribosomes bound to the beads according to the NucleoSpin RNA (input) and RNA Plus XS (pulldowns) kit manufacturer's recommendations.

**Library preparation, sequencing, and data analysis**

The library preparation was performed with poly-A purification for input samples and skipped poly-A for the pulldowns, both without rRNA depletion. The libraries were sequenced on Pair End, using an Illumina NovaSeq 6000 SP Whole sequencer, with 150 bp determined. All reads were analyzed by a quality control check using FASTQC, followed by trimming with Trimmomatic (Bolger et al., 2014), where unpaired reads and adaptor sequences were removed based on the quality scores. Then, another control quality check was performed.
Trimmed high-quality reads were aligned to the *Drosophila* genome (*Drosophila melanogaster*/dmel_r6.43_FB2021_06) using Hisat2 (Kim et al., 2015). The alignment files were sorted, indexed, and converted with Samtools to count reads with Htseq-Count (Anders et al., 2014). Library normalization and statistical analysis of differentially expressed genes (DEG) were analyzed by DESeq2 (Love et al., 2014), considering an adjusted *p*-value ≤ 0.05 and regularized logarithm (rLog) fold change smaller than -0.6 (down-regulated) or greater than 0.6 (up-regulated).
Gene Ontology (GO) term enrichment analysis for biological processes was performed with the Database for Annotation, Visualization, and Integrated Discovery (DAVID) 6.8 (Huang et al., 2009). Statistical analyses and data visualization were conducted in R using the base, dplyr, pheatmap, and ggplot2 packages.

**Comparative analysis with published data set**

For the comparative analysis with the mammalian data, transcripts with adjusted *p*-value ≤ 0.05 and log2 Fold Change > 0.6 (up-regulated) were selected from Table S6B (Jung et al., 2023). For rapid identification of orthologs, the list of the selected Ensembl Gene ID was analyzed with the *Drosophila* Integrative Ortholog Prediction Tool (DIOPT; http://www.flyrnai.org/diopt) (Hu et al., 2011). Only orthologs with high rank and best score were chosen to compare with our data set.

**Optogenetics-induced antennal grooming behavior**

Genetic crosses were performed in the darkness on standard cornmeal food in aluminum-covered vials supplemented with 200 μM all-trans retinoic acid (Hampel et al., 2015; Paglione et al., 2020). Optogenetic experiments to induce antennal grooming were conducted in the dark. Animals were visualized and recorded using an 850 nm infrared light source at an intensity of 2 mW/cm2 (Mightex, Toronto, CA). For CsChrimson activation, a 656 nm red-light source (Mightex) was used at 8 or 14 mW/cm$^2$ intensities. Animals were subjected to a 10 s 10 Hz red-light exposure, followed by a 30 s recovery phase where the red light was turned off. This repetition cycle was performed three times in total. Red light stimulus parameters were delivered with a NIDAQ board controlled through Bonsai (https://open-ephys.org/). Animals were manually scored using Noldus EthoVision XT software (Noldus Information

Technology), where grooming activity was plotted as the percentage of time spent grooming the antennae during red-light stimuli. The ablation of the antennae did not damage the rest of the head or lead to the mortality of the animals. Animals that died during the analysis window (7 dpa – 14 dpa) were excluded.

**Automated grooming detection system**

Frame-wise scoring of antennal grooming behavior was performed as an image-recognition task. Briefly, bouts of antennal grooming are a stereotypical pattern of foreleg movements directed toward the antennae that span several consecutive video frames. This pattern was captured and compressed on a single image by clipping the grooming episode over time and computing the pixel-wise standard deviation through the stack of frames. Supervised training of an artificial neural network was used to recognize these compressed images belonging to one of two categories: grooming or no-grooming. An end-to-end system was established that takes a raw video as input, and returns a frame-wise probability as output. Two neural networks and a set of image-processing functions wrapped in a single system were established requiring minimal user input. The details of the system together with the parameters used for training, validating, and testing are provided below.

**Network-1: Detection of the head and its fore region**

To simplify the task of detecting grooming events, the region of interest was restricted to the forehead of the animal and the region in front of it. A deconvolutional network was trained to detect the head of the animal and to output the coordinates of its centroid.

Model: The deconvolutional network was developed in Python (V 3.7.4) using the PyTorch Library (V 1.13.0). The network is composed of six layers: 3 convolutional layers (channels: 32, 64, 128; kernel size: 3, 5, 3; max pooling) and 6 deconvolutional layers (channels: 128, 64, 32; kernel size: 3, 5, 3;). The *Kaiming* weight initialization was used together with ReLU activation as implemented in the Pytorch library.

Dataset: Raw videos are large (1280 x 1024 px) grayscale *avi* files. To reduce processing time, the network was trained, validated, and tested on lower resolution (320 x 256 px) frames extracted from the video files and their relative binary mask of the head position in the video frame. 916 tuples (raw frame, binary mask) were used for training, 229 tuples for validation, and 250 tuples for testing the accuracy of the network.

Training, validation, and test: The network was trained to minimize the Mean Square Error loss function with the ADAM optimizer on batches of 8 tuples for 14 epochs. The learning rate was fixed at 0.003.

The coordinates of the binary mask's centroid was used to probe accuracy on the validation set. The Euclidean distance between the centroid of the binary mask and the max value of the

confidence map produced by the network is used to evaluate the accuracy of the segmentation process. The distance (average ± standard deviation) between centroids is 3.88 ± 3.48 pixels during validation and 4.33 ± 10.43 pixels in the test set.

The minimum diameter of an animal's head (e.g., side view relative to the camera) was estimated ~ 32 pixels. For this reason, a cut-off radius of 8 pixels (e.g., max distance between ground truth centroid and predicted centroid) was used to define the segmentation accuracy. According to this cut-off, the network correctly predicted the position of the head in 98.8 % of the test frames. The text file output of this network contained the frame-by-frame coordinates of the predicted position of the centroid of the head.

In addition, the inference script automatically detects the onset/offset of the red-light stimuli by first taking the average pixel intensity of a 100 x 50 pixel region surrounding the LED on the initial 200 frames (*light-off*) and then computing the z-score for each frame in the video. Frames that are 2 z-scores above the average are defined as *light-on* frames. This procedure leads to a marginal underestimation (5.4 frames, mean absolute difference, data not shown) of the total number of *light-on* frames as compared to the measure taken by a human observer.

**Network-2: Grooming detection**

The output of the deconvolutional network (e.g., the coordinates of the head's centroid) was used to define an ROI centered on the head of the animal and its fore region. Following this crop, the pixel-wise standard deviation of 10 consecutive frames was computed, and the network classified the resulting image as either grooming or no-grooming. A sliding window (*stride* = 1 frame) was applied to the input to compute the frame-wise probability of grooming on the full length of the raw video. The network was initially trained on naïve animals. However, the inference on animals that underwent injury (e.g., antennal ablation) was suboptimal. Therefore, the network was trained on two distinct datasets (e.g., animals with or without antennae), leading to two distinct sets of weights that were independently deployed according to the experimental group (e.g., before or after injury). The animal condition did not affect the quality of the inference on head tracking performed by the deconvolutional network.

<u>Model:</u> Pretrained ResNet50 (Pytorch: ResNet50_Weights.IMAGENET1K_V2) fine-tuned on our training datasets.

<u>Dataset:</u> Antennal grooming is defined as a stereotyped circular movement of the forelegs sweeping over the surface of the antennae. A trained experimenter manually labeled the grooming episodes using the *manual scoring module* of EthovisionXT16 (Noldus Information Technologies). This dataset represented the ground truth for training the ResNet50 and it required further processing before being used to train the network. First, the raw videos were processed with the deconvolutional network (see section "*detection of the head and its fore region*") to extract the coordinates of the head's centroid. Manual scoring of grooming events

together with the coordinates of the head centroid were used to clip grooming bouts and crop frames (128 x 128 px) on a region centered on the head of the animal. For each grooming bout, the pixel-wise standard deviation was computed on a stack of 10 consecutive frames taken with a sliding window (*stride* = 1) over the bout. A sequence of 10 frames was used to capture short bouts (camera fps: 15 Hz, ~0.7 seconds) of grooming. The same process was repeated for frames labeled as "*no_grooming*". These sets of images (e.g., *grooming* and *no_grooming*) were further inspected to remove images that could not be unambiguously attributed to one of the two categories. The images were then randomly allocated to one of three sets: train, validation, or test. Two distinct sets of images were obtained from the *before-* and *after-injury* conditions. The *before-injury* set comprised 30 subjects (number of frames, train = 3499, validation = 943, test = 64), while the after-injury comprised 22 subjects (train = 1615, validation = 413, test = 495).

Training, validation, and test: The ResNet50 was trained for 41 epochs with a Cross Entropy loss function, the ADAM optimizer, and a decaying learning rate (gamma = 0.1, 7 epochs). The classification accuracy on the validation and test sets was 95.9 % and 93.5 %, respectively.

**Post-processing of grooming prediction**

The ResNet50 outputs a text file containing the framewise probability values for grooming behavior. However, because of the projection through time (10 consecutive frames) of the training set and the sliding window ($n$ = 1), the probability value failed to capture sharp transitions between grooming states (e.g., onset-offset). For this reason, first, inference on the training set videos was run to get raw probability values; then these were binarized according to 7 probability threshold values θ ranging from 0.3 to 0.9 and for each frame with $p > \theta$, the 3 consecutive frames were labeled as 'grooming'. This procedure allowed to compensate for the bias introduced by the compression of 10 consecutive images without producing excess false positives. Finally, comparing the resulting grooming scores with manual scores allowed us to find an optimal probability threshold value that minimizes the difference between system and observer scores.

**Replication**

Unless stated otherwise, at least 3 biological replications were performed for all experiments for each genotype and/or condition.

**Software and statistics**

Image-J and Photoshop were used to process wing, *or22a*$^{+}$, *JO*$^{+}$ and *orco*$^{+}$ pictures. The optogenetics section includes the software used for the analysis. Unless stated otherwise, GraphPad Prism 9 was used to perform all the statistical analyses.

**Figure legend**

**Figure 1. Programmed axon degeneration-deficient olfactory and mechanosensory axons and their synapses remain circuit-integrated after injury. A** Examples of GFP-labeled axonal projections (arrow) of *or22a*$^{+}$ olfactory receptor neurons (ORN). Wild type and over-expression of dNmnat (*dnmnat*$^{OE}$), top and bottom, before and after injury (7 and 14 days post antennal ablation (dpa)), respectively. **B** Quantification of intact *or22a*$^{+}$ axons and total axonal and synaptic area; left and right, respectively. Data, average ± SEM ($n \geq 10$ brains). Unpaired two-tailed t-student test. **C** Examples of GFP-labeled *JO*$^{+}$ mechanosensory axonal projections. Wild type and *dnmnat*$^{OE}$; before and 7 and 14 dpa, respectively. **D** Quantification of intact *JO*$^{+}$ axons and total axonal and synaptic area. Scale bar, 20 µm. Data, average ± SEM ($n \geq 10$ brains). Unpaired two-tailed t-student test. **E** Robust preservation of circuit integrity in severed *dnmnat*$^{OE}$ projections. Quantification of manually scored evoked antennal grooming behavior in uninjured and injured animals. Data, % time of red-light stimuli ($n = 14$ animals). Three-way ANOVA with Tukey's multiple comparisons test. **F** Example of GFP-labeled wild-type and *dnmnat*$^{OE}$ olfactory receptor co-receptor (*orco*$^{+}$) axons and synapses before and 7 and 14 dpa. **G** Quantification of *orco*$^{+}$ intact axons (arrows) and projection area, respectively. Scale bar, 20 µm. Data, average ± SEM ($n \geq 5$ brains). Unpaired two-tailed t-student test. ****, $p < 0.0001$; *, $p < 0.05$.

**Figure 2. Identification of local translatomes in severed olfactory organ axons and synapses one week after injury. A** Translating ribosome affinity purification (TRAP) as a strategy to isolate *orco*$^{+}$ translatomes from severed axons and their synapses 7 dpa. **B** Heat map of 1033 differentially enriched transcripts between wild type and *dnmnat*$^{OE}$ 7 dpa (Z-Score average). **C** Gene ontology (GO) term enrichment analysis (biological processes) of 499 *dnmnat*$^{OE}$-enriched transcripts (fold change value > 0.6); sorted and plotted by *p*-value. **D** Heat map example of two significantly changed GO term groups, protein ubiquitination ($n = 16$) and calcium transport ($n = 9$), respectively. **E** Venn diagram of 499 *Drosophila dnmnat*$^{OE}$-enriched transcripts (TRAP) and 1058 mouse *Sarm1*$^{-/-}$ KO transcripts (axonal transcriptome; axotomized versus naive axons (Jung et al., 2023)). **F** GO term analysis (biological processes) of 61 enriched fly/mouse ortholog transcripts.

**Figure 3. Automated high-accuracy antennal grooming behavior detection system. A** Illustration of two-network system for head and antennal grooming detection (networks 1 and 2, respectively). **B** Examples of antennal grooming scores by the observer (absolute) and the system (probability); green and purple, top and bottom, respectively. Grey, 10 s 10 Hz red-light stimulus. **C** Mean absolute deviation of grooming detection between observer and system

(mean ± SEM, % time of red-light stimuli). **D** Linear regression of grooming detection by system and observer (% time of red-light stimuli; probability ≥ 0.3; $n = 24$ animals). **E** Grooming detection quantified by observer and system (% time of red-light stimuli, $n = 24$ animals). Paired two-tailed t-student test. **F** Mean absolute deviation between manual and automatic grooming detection after injury (7 dpa; mean ± SEM, % time of red-light stimuli). **G** Linear regression of grooming detection between observer and system at 7 dpa (% time of red-light stimuli; probability ≥ 0.4; $n = 18$ animals). **H** Grooming detection quantified by observer and system at 7 dpa (% time of red-light stimuli, $n = 9$ animals). Paired two-tailed t-student test; ns, $p > 0.05$.

**Figure 4. RNAi-mediated knockdown of candidates involved in protein ubiquitination and calcium transport reduces preserved circuit integrity one week after injury. A** RNAi-based strategy to identify candidates required for circuit integrity. **B** Screen of protein ubiquitination candidate genes. **C** Screen of calcium transport candidate genes. Data, % time of red-light stimuli ($n \geq 10$ animals). Paired two-tailed t-student and Two-Way ANOVA with Dunnett's multiple comparisons test; ****, $p < 0.0001$; ***, $p < 0.001$; **, $p < 0.01$; *, $p < 0.05$.

**Figure 5. RNAi-mediated knockdown of mTOR signaling candidates reduces preserved circuit integrity one week after injury. A** Protein synthesis mediated by the mTOR signaling pathway. Bold, candidates tested by RNAi. **B** RNAi targeting *raptor* and *s6k* result in reduced antennal grooming after injury. Data, % time of red-light stimuli ($n \geq 12$ animals). Paired two-tailed t-student test and Two-Way ANOVA with Dunnett's multiple comparisons test; ****, $p < 0.0001$; *, $p < 0.05$.

**Supplementary figure legend**

**Supplementary figure 1. Olfactory organ projections as a large-scale resource to express and detect GFP-tagged ribosomal protein 10Ab. A** Western blots of *Drosophila* heads with tissue-specifically expressed GFP-tagged ribosomal protein 10Ab (GFP::RpL10Ab). 4 heads/lane. Arrow, molecular weight of GFP::RpL10Ab. **B** Quantification of GFP immunoreactivity by densitometry. Data, mean ± SEM ($n$ = 3, three replicates of three biological experiments). Arbitrary units, A.U.; One-way ANOVA with Tukey's multiple comparisons test; ****, $p < 0.0001$; ns (not significant), $p > 0.05$.

**Supplementary figure 2. Heat maps of biological process GO terms significantly enriched in *dnmnat$^{OE}$* 7 dpa. A** Heat map of oxidation/reduction process transcripts ($n$ = 30). **B** Heat map of axon guidance and extension transcripts ($n$ = 24). **C** Heat map of G-protein receptor transcripts ($n$ = 13). **D** Heat map of transmembrane transport transcripts ($n$ = 30). **E** Heat map of vesicle-mediated transport transcripts ($n$ = 19). **F** Heat map of autophagy transcripts ($n$ = 6). **G** Heat map of RNA processing transcripts ($n$ = 6). Expression levels, Z-Score average.

**Supplementary figure 3. Background filtering of transcriptional profiles. A** Strategy implemented for background filtering. **B** Heat map of 1351 transcripts differentially expressed in wild type (*orco > GFP::RpL10Ab*) compared to background (*orco–Gal4*) 7 dpa. **C** Heat map of 1461 transcripts differentially expressed in *dnmnat$^{OE}$* (*orco > GFP::RpL10Ab*, *dnmnat*) compared to background (*orco–Gal4*) 7 dpa. **D** Heat map of 1033 transcripts differentially expressed in *dnmnat$^{OE}$* (*orco > GFP::RpL10Ab*, *dnmnat*) compared to wild type (*orco > GFP::RpL10Ab*) 7 dpa. Data, Z-Score average. **E** Venn diagram of 750 transcripts enriched in wild type (compared to background), 751 transcripts enriched in *dnmnat$^{OE}$* (compared to background), and 499 transcripts enriched in *dnmnat$^{OE}$* (compared to wild type) 7 dpa. **F** Biological process GO term analysis of 165 enriched transcripts in *dnmnat$^{OE}$* after background filtering (fold change value > 0.6); sorted and plotted by $p$-value.

**Supplementary figure 4. Scoring variability of antennal grooming between system and observers.** Standard deviation between scores given by each observer to the same animal. The plot illustrates the similarity between the standard deviations of observer 1 versus the system and observer 2 versus the system, as compared to the standard deviation observed among observers (horizontal black line; median values - the unit is the number of frames). Non-parametric one-way ANOVA (Kruskal-Wallis test) with Dunn multiple comparisons test; ns (not statistically significant), $p > 0.05$.

**Supplementary figure 5. Detection of temperature-dependent changes in antennal grooming.** Quantification of antennal grooming detection by observer and system in wild-type flies with CsChrimson expressed in JO neurons of 7-day-old animals (green and purple, respectively; probability, ≥ 0.3; % time of red-light stimuli; $n$ = 6 animals). Three-way ANOVA; *, $p < 0.05$.

**Supplementary figure 6. Time-course of optogenetic-induced antennal grooming after eclosion.** Quantification of antennal grooming detection by system in wild-type flies with CsChrimson expressed in JO neurons between 0 to 7 days post eclosion (dpe). Probability, ≥ 0.3 ($n$ = 7 animals). One-way ANOVA with Turkey's multiple comparisons test; **, $p < 0.01$; *, $p < 0.05$.

**Supplementary figure 7. RNAi-based screen of protein ubiquitination candidates that are likely not required for circuit integrity.** Quantification of automated antennal grooming scores before and 7 dpa (% time of red-light stimuli, $n \geq 10$ animals). Paired two-tailed t-student test and Two-Way ANOVA with Dunnett's multiple comparisons test. Data, not statistically significant.

**Supplementary figure 8. RNAi-based screen of calcium transport candidates. A** Quantification of automated antennal grooming scores before and 7 dpa. Data, not statistically significant**. B** Validation of *nckx30C* by two different RNAi lines (#1 and #2, respectively). Data, % time of red-light stimuli ($n \geq 10$ animals). Paired two-tailed t-student and Two-Way ANOVA with Dunnett's multiple comparisons test; ****, $p < 0.0001$; **, $p < 0.01$; *, $p < 0.05$.

**Video legend**

**Video 1. Example of automated antennal grooming detection of a wild-type animal.** Left, recording of animal in arena exposed to red-light stimulus indicated by flashing diode (bottom). Square, network 1 head detection. Top right, network 2 antennal grooming detection (probability indicated in the upper left corner). Bottom right, probability plot. Wild-type animal expressing CsChrimson in JO neurons.

**Video 2. Example of automated antennal grooming detection of a wild-type animal after injury.** Left, recording of animal in arena exposed to red-light stimulus indicated by flashing diode (bottom). Square, network 1 head detection. Top right, network 2 antennal grooming detection (probability indicated in the upper left corner). Bottom right, probability plot. Wild-type animal expressing CsChrimson in JO neurons 7 dpa.

**Video 3. Example of automated antennal grooming detection of an animal expressing *dnmnat* in JO neurons after injury.** Left, recording of animal in arena exposed to red-light stimulus indicated by flashing diode (bottom). Square, network 1 head detection. Top right, network 2 antennal grooming detection (probability indicated in the upper left corner). Bottom right, probability plot. Wild-type animal expressing CsChrimson and *dnmnat* in JO neurons 7 dpa.

**References**


Anders, S., Pyl, P. T., & Huber, W. (2014). HTSeq—a Python framework to work with high-throughput sequencing data | Bioinformatics | Oxford Academic. *Bioinformatics*, *31*(2).

Augustus Volney Waller. (1850). XX. Experiments on the section of the glossopharyngeal and hypoglossal nerves of the frog, and observations of the alterations produced thereby in the structure of their primitive fibres. *Philosophical Transactions of the Royal Society of London*, *140*, 423–429. https://doi.org/10.1098/rstl.1850.0021

Bolger, A. M., Lohse, M., & Usadel, B. (2014). Trimmomatic: A flexible trimmer for Illumina sequence data. *Bioinformatics*, *30*(15). https://doi.org/10.1093/bioinformatics/btu170

Brazill, J. M., Li, C., Zhu, Y., & Zhai, R. G. (2017). NMNAT: It's an NAD+ synthase… It's a chaperone… It's a neuroprotector. In *Current Opinion in Genetics and Development* (Vol. 44). https://doi.org/10.1016/j.gde.2017.03.014

Coleman, M. P., & Höke, A. (2020). Programmed axon degeneration: from mouse to mechanism to medicine. In *Nature Reviews Neuroscience* (Vol. 21, Issue 4). https://doi.org/10.1038/s41583-020-0269-3

Court, F. A., Hendriks, W. T. J., MacGillavry, H. D., Alvarez, J., & Van Minnen, J. (2008). Schwann cell to axon transfer of ribosomes: Toward a novel understanding of the role of glia in the nervous system. *Journal of Neuroscience*, *28*(43). https://doi.org/10.1523/JNEUROSCI.2429-08.2008

Ding, Q., Cecarini, V., & Keller, J. N. (2007). Interplay between protein synthesis and degradation in the CNS: physiological and pathological implications. In *Trends in Neurosciences* (Vol. 30, Issue 1). https://doi.org/10.1016/j.tins.2006.11.003

Ederle, H., & Dormann, D. (2017). TDP-43 and FUS en route from the nucleus to the cytoplasm. In *FEBS Letters* (Vol. 591, Issue 11). https://doi.org/10.1002/1873-3468.12646

Fang, Y., Soares, L., Teng, X., Geary, M., & Bonini, N. M. (2012). A novel drosophila model of nerve injury reveals an essential role of Nmnat in maintaining axonal integrity. *Current Biology*, *22*(7). https://doi.org/10.1016/j.cub.2012.01.065

Geisler, S., Doan, R. A., Cheng, G. C., Cetinkaya-Fisgin, A., Huang, S. X., Höke, A., Milbrandt, J., & DiAntonio, A. (2019). Vincristine and bortezomib use distinct upstream mechanisms to activate a common SARM1-dependent axon degeneration program. *JCI Insight*, *4*(17). https://doi.org/10.1172/jci.insight.129920

Gilley, J., & Coleman, M. P. (2010). Endogenous Nmnat2 Is an Essential Survival Factor for Maintenance of Healthy Axons. *PLoS Biology*, *8*(1). https://doi.org/10.1371/journal.pbio.1000300

Glock, C., Biever, A., Tushev, G., Nassim-Assir, B., Kao, A., Bartnik, I., Dieck, S. tom, & Schuman, E. M. (2021). The translatome of neuronal cell bodies, dendrites, and axons. *Proceedings of the National Academy of Sciences of the United States of America*, *118*(43). https://doi.org/10.1073/pnas.2113929118

Gumy, L. F., Yeo, G. S. H., Tung, Y. C. L., Zivraj, K. H., Willis, D., Coppola, G., Lam, B. Y. H., Twiss, J. L., Holt, C. E., & Fawcett, J. W. (2011). Transcriptome analysis of embryonic

and adult sensory axons reveals changes in mRNA repertoire localization. *RNA*, *17*(1). https://doi.org/10.1261/rna.2386111

Hafner, A. S., Donlin-Asp, P. G., Leitch, B., Herzog, E., & Schuman, E. M. (2019). Local protein synthesis is a ubiquitous feature of neuronal pre- And postsynaptic compartments. *Science*, *364*(6441). https://doi.org/10.1126/science.aau3644

Hampel, S., Franconville, R., Simpson, J. H., & Seeds, A. M. (2015). A neural command circuit for grooming movement control. *ELife*, *4*(September). https://doi.org/10.7554/eLife.08758

Hampel, S., McKellar, C. E., Simpson, J. H., & Seeds, A. M. (2017). Simultaneous activation of parallel sensory pathways promotes a grooming sequence in drosophila. *ELife*, *6*. https://doi.org/10.7554/eLife.28804

Holt, C. E., Martin, K. C., & Schuman, E. M. (2019). Local translation in neurons: visualization and function. In *Nature Structural and Molecular Biology* (Vol. 26, Issue 7). https://doi.org/10.1038/s41594-019-0263-5

Hu, Y., Flockhart, I., Vinayagam, A., Bergwitz, C., Berger, B., Perrimon, N., & Mohr, S. E. (2011). An integrative approach to ortholog prediction for disease-focused and other functional studies. *BMC Bioinformatics*, *12*. https://doi.org/10.1186/1471-2105-12-357

Huang, D. W., Sherman, B. T., & Lempicki, R. A. (2009). Systematic and integrative analysis of large gene lists using DAVID bioinformatics resources. *Nature Protocols*, *4*(1). https://doi.org/10.1038/nprot.2008.211

Huppke, P., Wegener, E., Gilley, J., Angeletti, C., Kurth, I., Drenth, J. P. H., Stadelmann, C., Barrantes-Freer, A., Brück, W., Thiele, H., Nürnberg, P., Gärtner, J., Orsomando, G., & Coleman, M. P. (2019). Homozygous NMNAT2 mutation in sisters with polyneuropathy and erythromelalgia. *Experimental Neurology*, *320*. https://doi.org/10.1016/j.expneurol.2019.112958

Ishiguro, A., Kimura, N., Watanabe, Y., Watanabe, S., & Ishihama, A. (2016). TDP-43 binds and transports G-quadruplex-containing mRNAs into neurites for local translation. *Genes to Cells*, *21*(5). https://doi.org/10.1111/gtc.12352

Iwata, A., Stys, P. K., Wolf, J. A., Chen, X. H., Taylor, A. G., Meaney, D. F., & Smith, D. H. (2004). Traumatic axonal injury induces proteolytic cleavage of the voltage-gated sodium channels modulated by tetrodotoxin and protease inhibitors. *Journal of Neuroscience*, *24*(19). https://doi.org/10.1523/JNEUROSCI.0515-03.2004

Jarome, T. J., & Helmstetter, F. J. (2014). Protein degradation and protein synthesis in long-term memory formation. In *Frontiers in Molecular Neuroscience* (Vol. 7, Issue JUNE). https://doi.org/10.3389/fnmol.2014.00061

Jung, J., Ohk, J., Kim, H., Holt, C. E., Park, H. J., & Jung, H. (2023). mRNA transport, translation, and decay in adult mammalian central nervous system axons. *Neuron*, *111*(5), 650-668.e4. https://doi.org/10.1016/j.neuron.2022.12.015

Kim, D., Langmead, B., & Salzberg, S. L. (2015). HISAT: A fast spliced aligner with low memory requirements. *Nature Methods*, *12*(4). https://doi.org/10.1038/nmeth.3317

Krauss, R., Bosanac, T., Devraj, R., Engber, T., & Hughes, R. O. (2020). Axons Matter: The Promise of Treating Neurodegenerative Disorders by Targeting SARM1-Mediated

Axonal Degeneration. In *Trends in Pharmacological Sciences* (Vol. 41, Issue 4). https://doi.org/10.1016/j.tips.2020.01.006

Lee, T., & Luo, L. (1999). Mosaic analysis with a repressible neurotechnique cell marker for studies of gene function in neuronal morphogenesis. *Neuron*, *22*(3). https://doi.org/10.1016/S0896-6273(00)80701-1

Llobet Rosell, A., & Neukomm, L. J. (2019). Axon death signalling in Wallerian degeneration among species and in disease. In *Open Biology* (Vol. 9, Issue 8). https://doi.org/10.1098/rsob.190118

Llobet Rosell, A., Paglione, M., Gilley, J., Kocia, M., Perillo, G., Gasparrini, M., Cialabrini, L., Raffaelli, N., Angeletti, C., Orsomando, G., Wu, P. H., Coleman, M. P., Loreto, A., & Neukomm, L. J. (2022). The NAD+ precursor NMN activates dSarm to trigger axon degeneration in Drosophila. *ELife*, *11*. https://doi.org/10.7554/ELIFE.80245

Love, M. I., Huber, W., & Anders, S. (2014). Moderated estimation of fold change and dispersion for RNA-seq data with DESeq2. *Genome Biology*, *15*(12). https://doi.org/10.1186/s13059-014-0550-8

Lukacs, M., Gilley, J., Zhu, Y., Orsomando, G., Angeletti, C., Liu, J., Yang, X., Park, J., Hopkin, R. J., Coleman, M. P., Zhai, R. G., & Stottmann, R. W. (2019). Severe biallelic loss-of-function mutations in nicotinamide mononucleotide adenylyltransferase 2 (NMNAT2) in two fetuses with fetal akinesia deformation sequence. *Experimental Neurology*, *320*. https://doi.org/10.1016/j.expneurol.2019.112961

Lunn, E. R., Perry, V. H., Brown, M. C., Rosen, H., & Gordon, S. (1989). Absence of Wallerian Degeneration does not Hinder Regeneration in Peripheral Nerve. *European Journal of Neuroscience*, *1*(1). https://doi.org/10.1111/j.1460-9568.1989.tb00771.x

MacDonald, J. M., Beach, M. G., Porpiglia, E., Sheehan, A. E., Watts, R. J., & Freeman, M. R. (2006). The Drosophila Cell Corpse Engulfment Receptor Draper Mediates Glial Clearance of Severed Axons. *Neuron*, *50*(6). https://doi.org/10.1016/j.neuron.2006.04.028

Mack, T. G. A., Reiner, M., Beirowski, B., Mi, W., Emanuelli, M., Wagner, D., Thomson, D., Gillingwater, T., Court, F., Conforti, L., Fernando, F. S., Tarlton, A., Andressen, C., Addicks, K., Magni, G., Ribchester, R. R., Perry, V. H., & Coleman, M. P. (2001). Wallerian degeneration of injured axons and synapses is delayed by a Ube4b/Nmnat chimeric gene. *Nature Neuroscience*, *4*(12). https://doi.org/10.1038/nn770

Maday, S., Twelvetrees, A. E., Moughamian, A. J., & Holzbaur, E. L. F. (2014). Axonal Transport: Cargo-Specific Mechanisms of Motility and Regulation. In *Neuron* (Vol. 84, Issue 2). https://doi.org/10.1016/j.neuron.2014.10.019

Mariano, V., Domínguez-Iturza, N., Neukomm, L. J., & Bagni, C. (2018). Maintenance mechanisms of circuit-integrated axons. In *Current Opinion in Neurobiology* (Vol. 53). https://doi.org/10.1016/j.conb.2018.08.007

Neukomm, L. J., Burdett, T. C., Seeds, A. M., Hampel, S., Coutinho-Budd, J. C., Farley, J. E., Wong, J., Karadeniz, Y. B., Osterloh, J. M., Sheehan, A. E., & Freeman, M. R. (2017). Axon Death Pathways Converge on Axundead to Promote Functional and Structural Axon Disassembly. *Neuron*, *95*(1). https://doi.org/10.1016/j.neuron.2017.06.031

Osterloh, J. M., Yang, J., Rooney, T. M., Fox, A. N., Adalbert, R., Powell, E. H., Sheehan, A. E., Avery, M. A., Hackett, R., Logan, M. A., MacDonald, J. M., Ziegenfuss, J. S., Milde, S., Hou, Y. J., Nathan, C., Ding, A., Brown, R. H., Conforti, L., Coleman, M., … Freeman, M. R. (2012). dSarm/Sarm1 is required for activation of an injury-induced axon death pathway. *Science*, *337*(6093). https://doi.org/10.1126/science.1223899

Ostroff, L. E., Santini, E., Sears, R., Deane, Z., Kanadia, R. N., Ledoux, J. E., Lhakhang, T., Tsirigos, A., Heguy, A., & Klann, E. (2019). Axon TRAP reveals learning-associated alterations in cortical axonal mRNAs in the lateral amgydala. *ELife*, *8*. https://doi.org/10.7554/eLife.51607

Paglione, M., Llobet Rosell, A., Chatton, J. Y., & Neukomm, L. J. (2020). Morphological and Functional Evaluation of Axons and their Synapses during Axon Death in Drosophila melanogaster. *J. Vis. Exp*, *157*, 60865. https://doi.org/10.3791/60865

Patrick, G. N. (2006). Synapse formation and plasticity: Recent insights from the perspective of the ubiquitin proteasome system. In *Current Opinion in Neurobiology* (Vol. 16, Issue 1). https://doi.org/10.1016/j.conb.2006.01.007

Raiders, S., Han, T., Scott-Hewitt, N., Kucenas, S., Lew, D., Logan, M. A., & Singhvi, A. (2021). Engulfed by glia: Glial pruning in development, function, and injury across species. *Journal of Neuroscience*, *41*(5). https://doi.org/10.1523/JNEUROSCI.1660-20.2020

Rishal, I., & Fainzilber, M. (2014). Axon-soma communication in neuronal injury. In *Nature Reviews Neuroscience* (Vol. 15, Issue 1). https://doi.org/10.1038/nrn3609

Rozenbaum, M., Rajman, M., Rishal, I., Koppel, I., Koley, S., Medzihradszky, K. F., Oses-Prieto, J. A., Kawaguchi, R., Amieux, P. S., Burlingame, A. L., Coppola, G., & Fainzilber, M. (2018). Translatome regulation in neuronal injury and axon regrowth. *ENeuro*, *5*(2). https://doi.org/10.1523/ENEURO.0276-17.2018

Sapar, M. L., & Han, C. (2019). Die in pieces: How Drosophila sheds light on neurite degeneration and clearance. In *Journal of Genetics and Genomics* (Vol. 46, Issue 4). https://doi.org/10.1016/j.jgg.2019.03.010

Shigeoka, T., Jung, H., Jung, J., Turner-Bridger, B., Ohk, J., Lin, J. Q., Amieux, P. S., & Holt, C. E. (2016). Dynamic Axonal Translation in Developing and Mature Visual Circuits. *Cell*, *166*(1). https://doi.org/10.1016/j.cell.2016.05.029

Stirling, D. P., & Stys, P. K. (2010). Mechanisms of axonal injury: internodal nanocomplexes and calcium deregulation. In *Trends in Molecular Medicine* (Vol. 16, Issue 4). https://doi.org/10.1016/j.molmed.2010.02.002

Terenzio, M., Koley, S., Samra, N., Rishal, I., Zhao, Q., Sahoo, P. K., Urisman, A., Marvaldi, L., Oses-Prieto, J. A., Forester, C., Gomes, C., Kalinski, A. L., Di Pizio, A., Doron-Mandel, E., Perry, R. B. T., Koppel, I., Twiss, J. L., Burlingame, A. L., & Fainzilber, M. (2018). Locally translated mTOR controls axonal local translation in nerve injury. *Science*, *359*(6382). https://doi.org/10.1126/science.aan1053

Thelen, M. P., & Kye, M. J. (2020). The Role of RNA Binding Proteins for Local mRNA Translation: Implications in Neurological Disorders. In *Frontiers in Molecular Biosciences* (Vol. 6). https://doi.org/10.3389/fmolb.2019.00161

Thomas, A., Lee, P. J., Dalton, J. E., Nomie, K. J., Stoica, L., Costa-Mattioli, M., Chang, P., Nuzhdin, S., Arbeitman, M. N., & Dierick, H. A. (2012). A versatile method for cell-

specific profiling of translated mrnas in Drosophila. *PLoS ONE*, *7*(7). https://doi.org/10.1371/journal.pone.0040276

Vosshall, L. B., Wong, A. M., & Axel, R. (2000). An olfactory sensory map in the fly brain. *Cell*, *102*(2). https://doi.org/10.1016/S0092-8674(00)00021-0

Wang, J. W., Wong, A. M., Flores, J., Vosshall, L. B., & Axel, R. (2003). Two-photon calcium imaging reveals an odor-evoked map of activity in the fly brain. *Cell*, *112*(2). https://doi.org/10.1016/S0092-8674(03)00004-7

Wang, X., & Proud, C. G. (2006). The mTOR pathway in the control of protein synthesis. In *Physiology* (Vol. 21, Issue 5, pp. 362–369). https://doi.org/10.1152/physiol.00024.2006

Wedel, M. J. (2012). A monument of inefficiency: The presumed course of the recurrent laryngeal nerve in sauropod dinosaurs. *Acta Palaeontologica Polonica*, *57*(2). https://doi.org/10.4202/app.2011.0019

Xiong, X., Hao, Y., Sun, K., Li, J., Li, X., Mishra, B., Soppina, P., Wu, C., Hume, R. I., & Collins, C. A. (2012). The Highwire Ubiquitin Ligase Promotes Axonal Degeneration by Tuning Levels of Nmnat Protein. *PLoS Biology*, *10*(12). https://doi.org/10.1371/journal.pbio.1001440

Yoon, B. C., Jung, H., Dwivedy, A., O'Hare, C. M., Zivraj, K. H., & Holt, C. E. (2012). Local translation of extranuclear lamin B promotes axon maintenance. *Cell*, *148*(4). https://doi.org/10.1016/j.cell.2011.11.064

Zhai, R. G., Cao, Y., Hiesinger, P. R., Zhou, Y., Mehta, S. Q., Schulze, K. L., Verstreken, P., & Bellen, H. J. (2006). Drosophila NMNAT maintains neural integrity independent of its NAD synthesis activity. *PLoS Biology*, *4*(12). https://doi.org/10.1371/journal.pbio.0040416

Zhai, R. G., Rizzi, M., & Garavaglia, S. (2009). Nicotinamide/nicotinic acid mononucleotide adenylyltransferase, new insights into an ancient enzyme. In *Cellular and Molecular Life Sciences* (Vol. 66, Issue 17). https://doi.org/10.1007/s00018-009-0047-x

Zhulyn, O., Rosenblatt, H. D., Shokat, L., Dai, S., Kuzuoglu-Öztürk, D., Zhang, Z., Ruggero, D., Shokat, K. M., & Barna, M. (2023). Evolutionarily divergent mTOR remodels translatome for tissue regeneration. *Nature*, *620*(7972), 163–171. https://doi.org/10.1038/s41586-023-06365-1

Paglione *et al.*, Figure 1

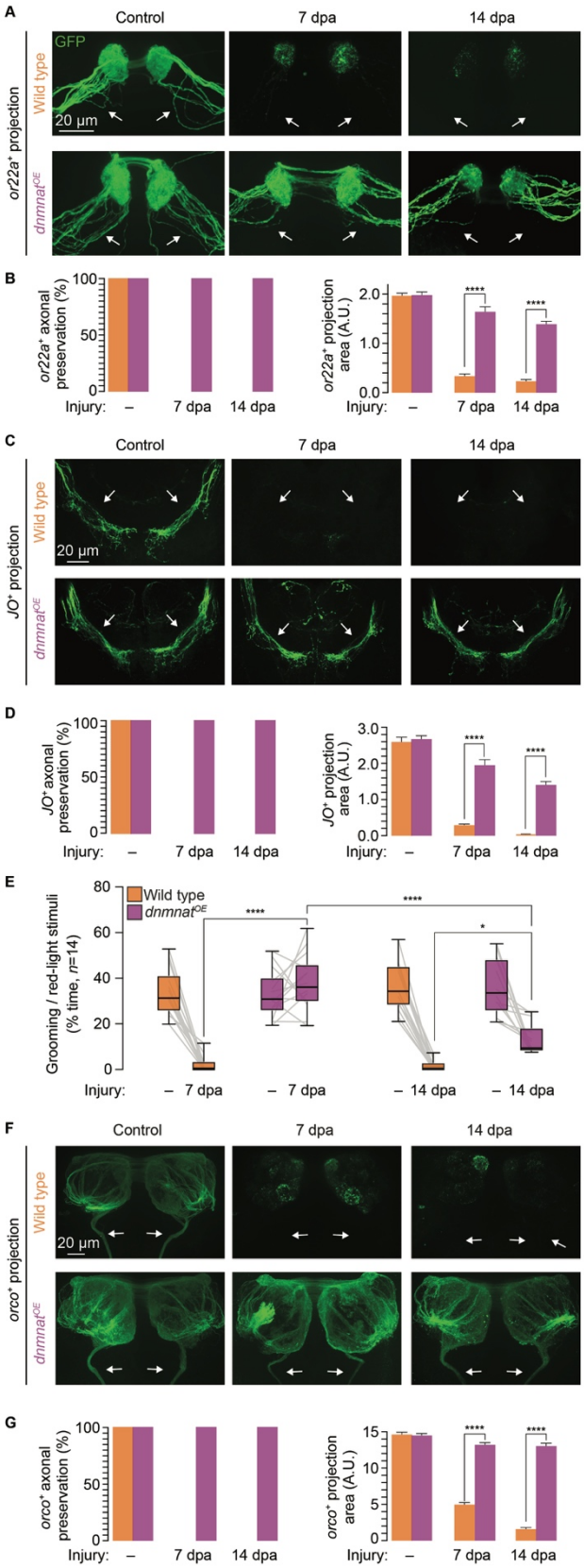

Paglione *et al.*, Figure 2

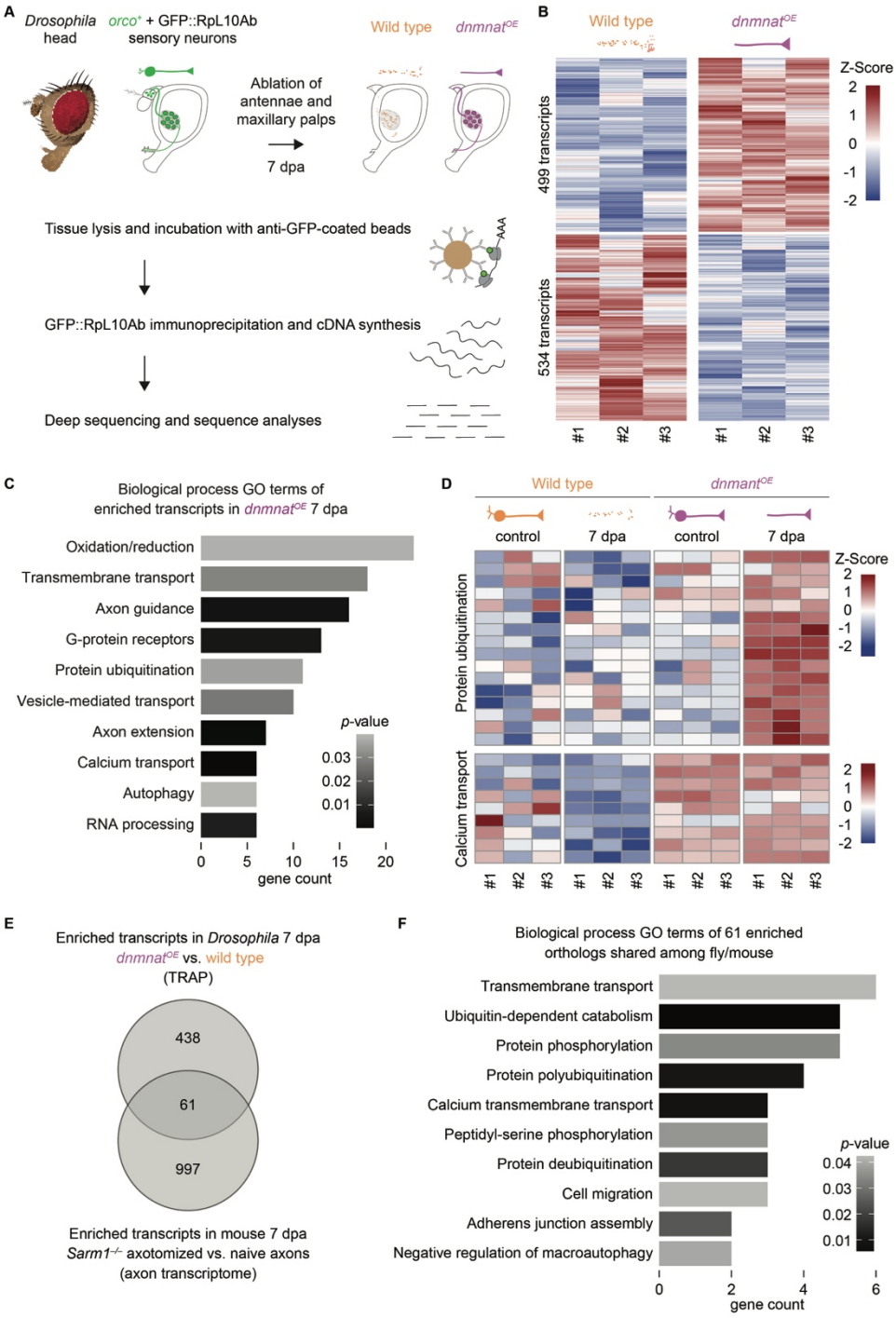

Paglione *et al.*, Figure 3

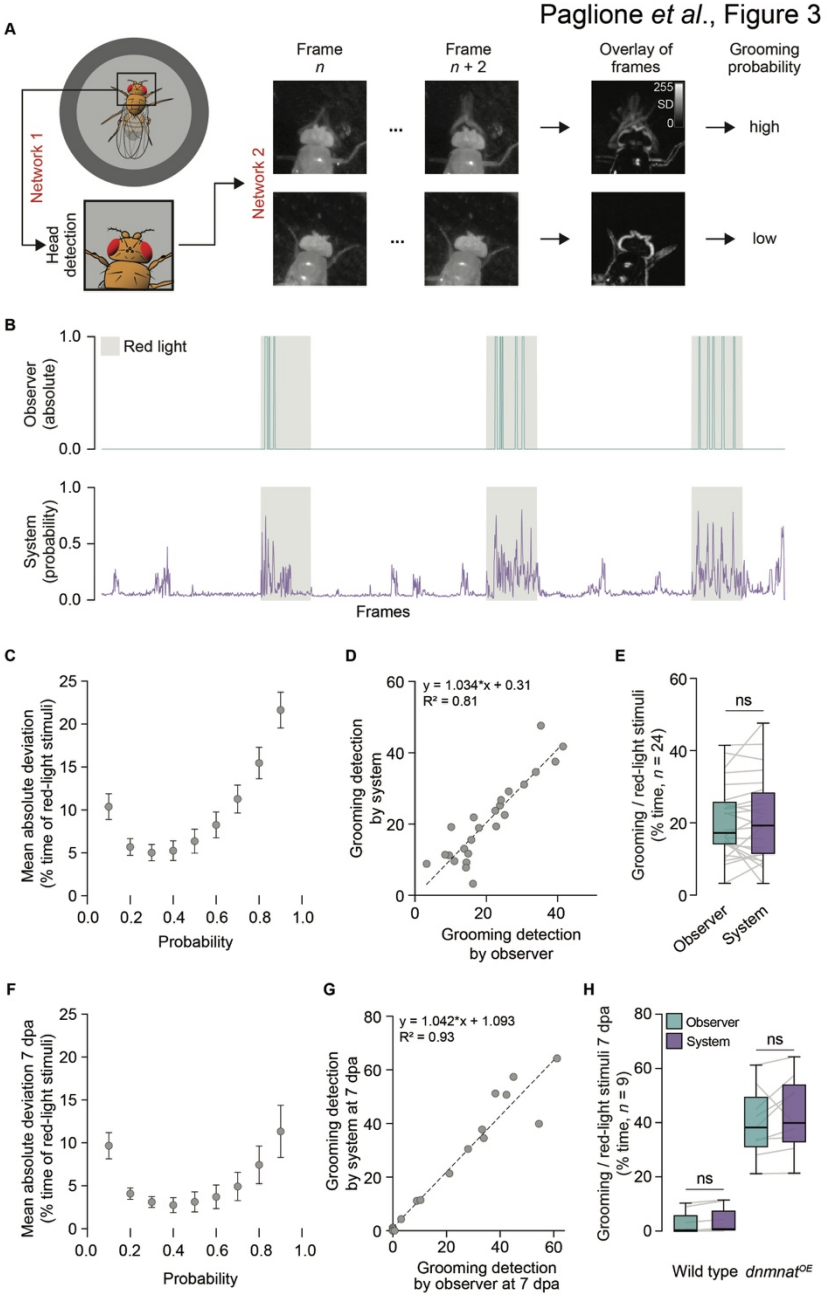

Paglione *et al.*, Figure 4

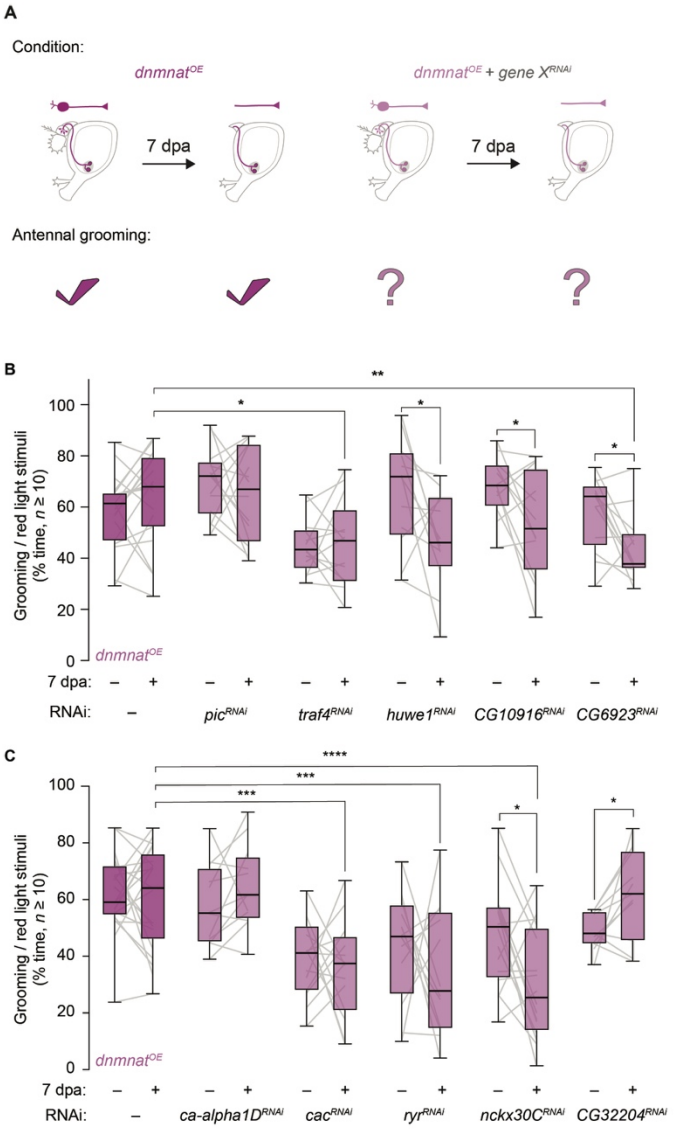

Paglione *et al.*, Figure 5

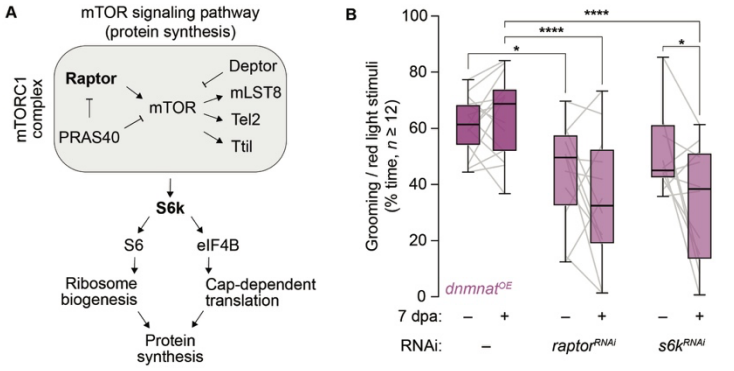

Paglione *et al*., Supplementary figure 1

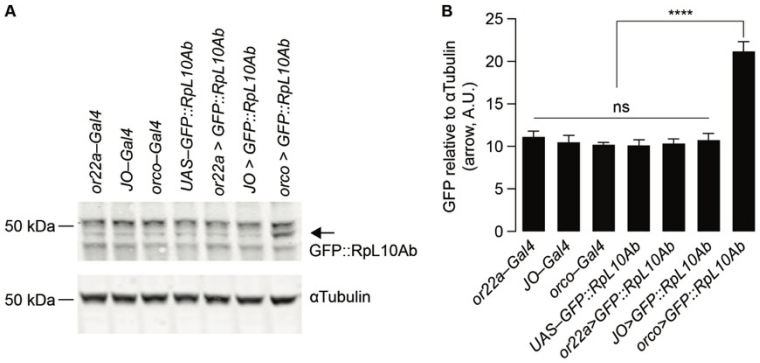

Paglione *et al.*, Supplementary figure 2

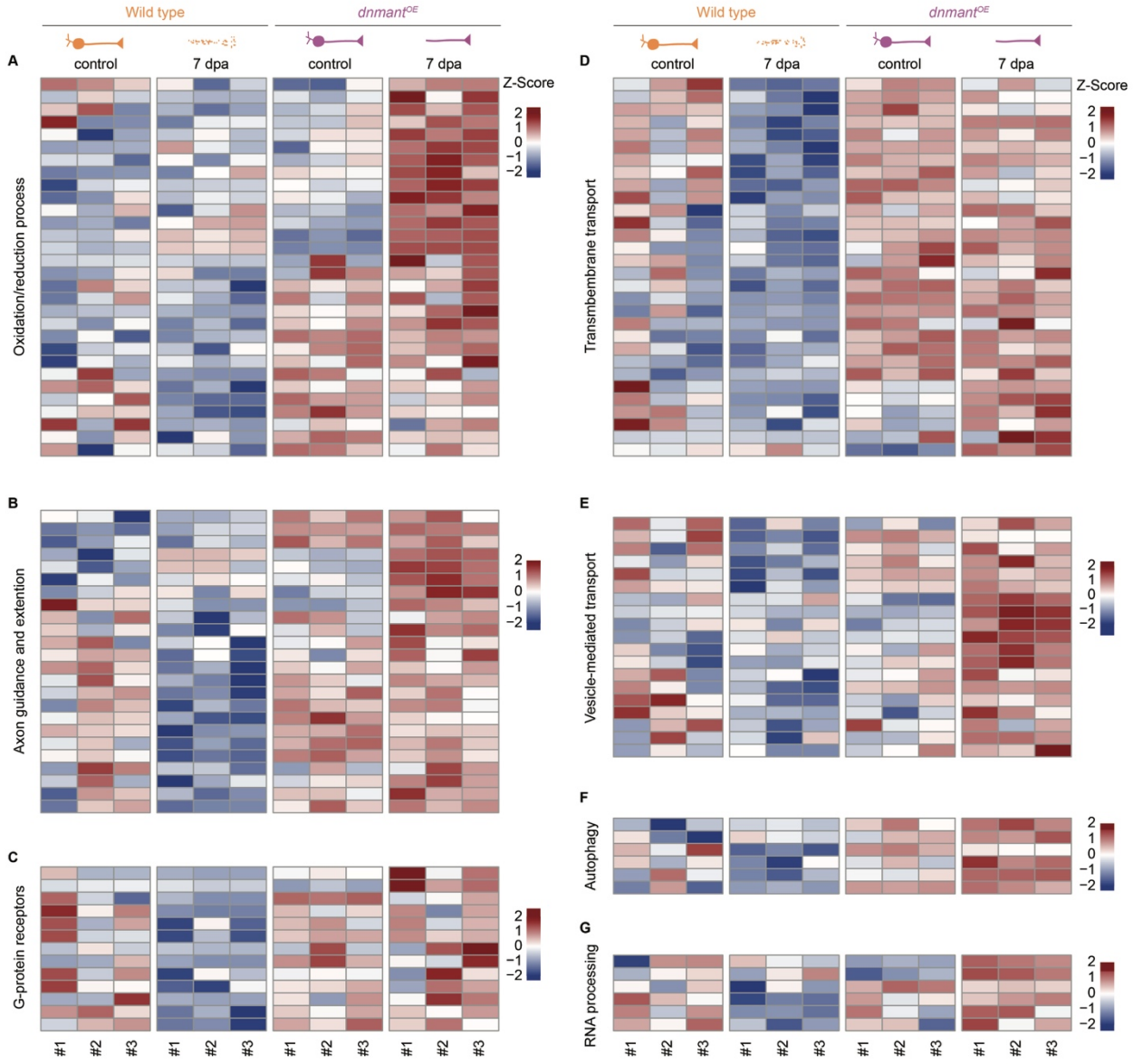

Paglione *et al.*, Supplementary figure 3

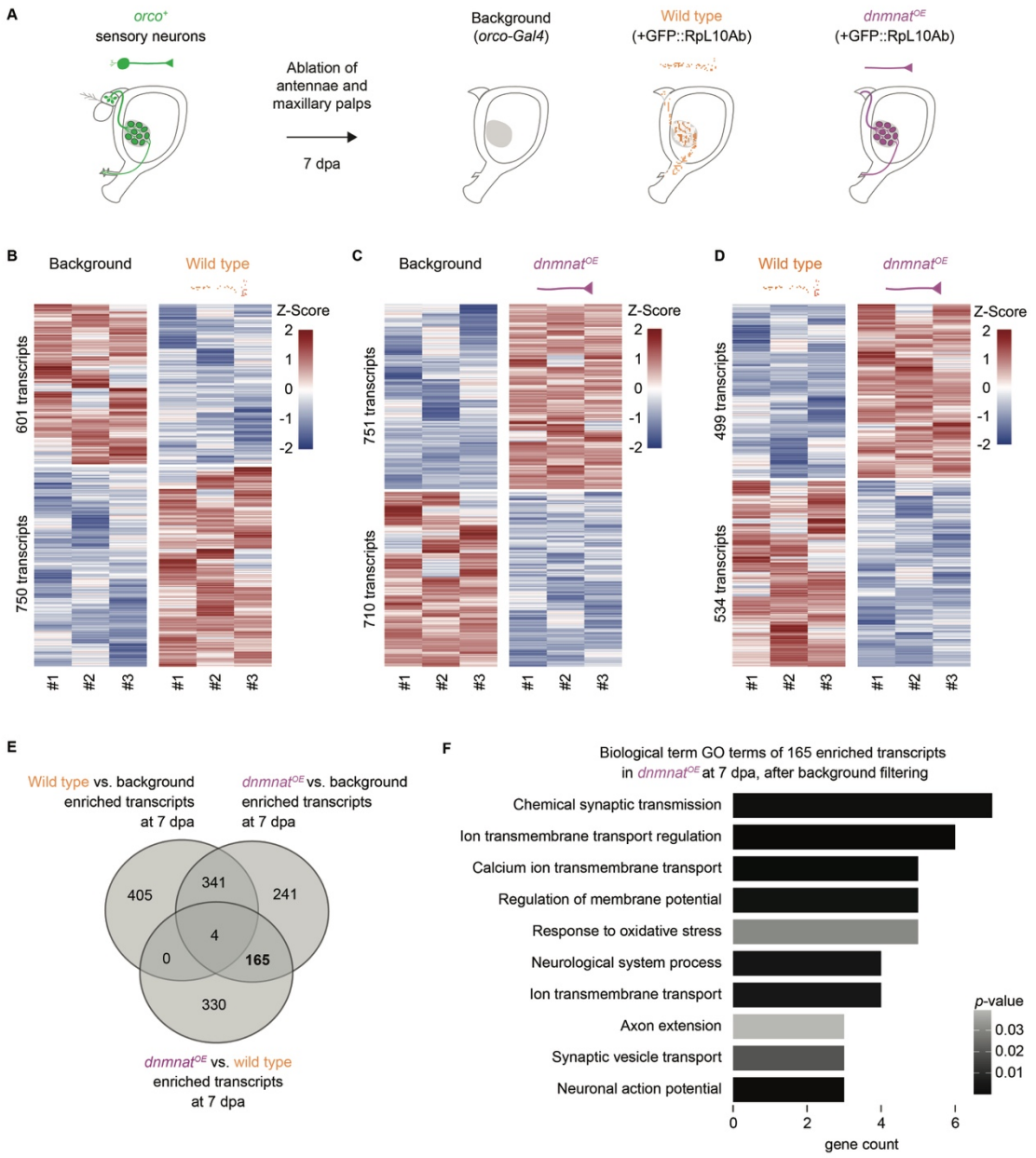

Paglione *et al*., Supplementary figure 4

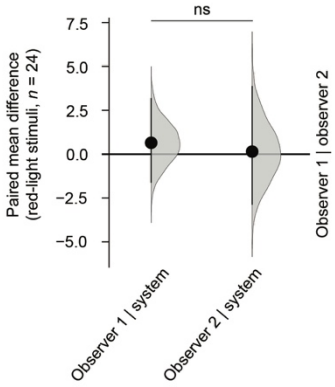

Paglione *et al*., Supplementary figure 5

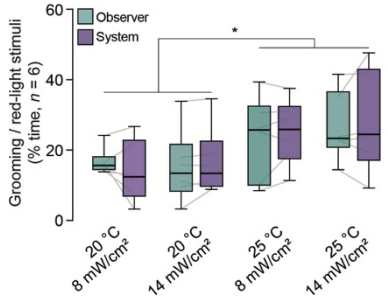

Paglione *et al*., Supplementary figure 6

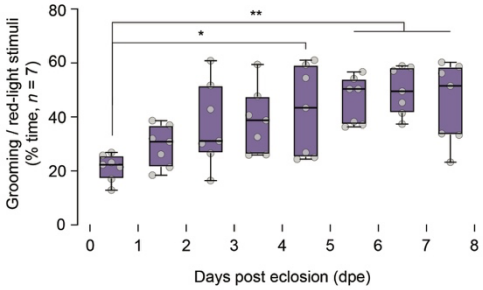

Paglione *et al*., Supplementary figure 7

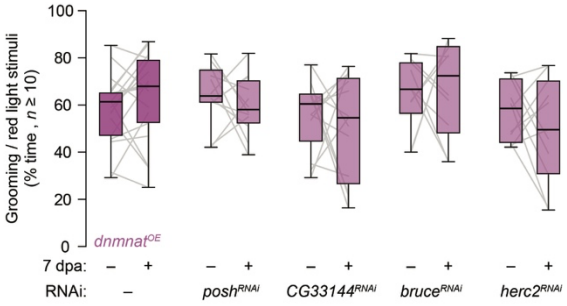
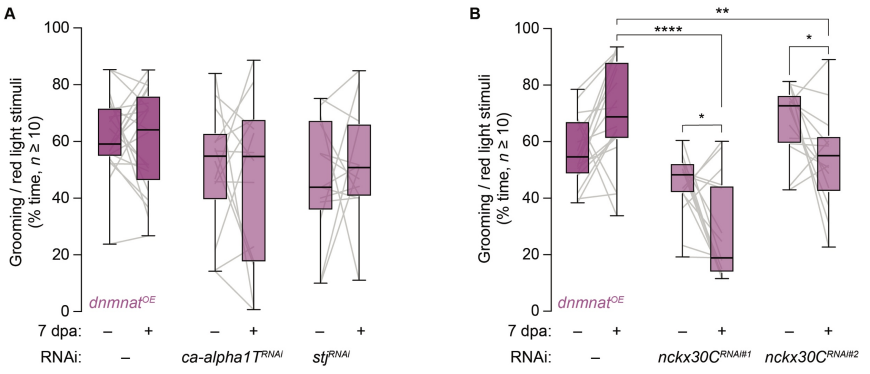
Paglione *et al*., Supplementary figure 8